Evaluation of the carbon cycle components in the Norwegian Earth System Model (NorESM)

J. F. Tjiputra[1,2,3]**, C. Roelandt**[1,3]**, M. Bentsen**[2,3]**, D. M. Lawrence**[4]**, T. Lorentzen**[2,3]**, J. Schwinger**[1,3]**, Ø. Seland**[5]**, and C. Heinze**[1,2,3]

[1]University of Bergen, Geophysical Institute, Bergen, Norway
[2]Uni Bjerknes Centre, Uni Research, Bergen, Norway
[3]Bjerknes Centre for Climate Research, Bergen, Norway
[4]National Center for Atmospheric Research, Boulder, Colorado, USA
[5]Norwegian Meteorological Institute, Oslo, Norway

Correspondence to: J. F. Tjiputra (jerry.tjiputra@bjerknes.uib.no)

Abstract

The recently developed Norwegian Earth System Model (NorESM) is employed for simulations contributing to the CMIP5 (Coupled Model Intercomparison Project phase 5) experiments and the fifth assessment report of the Intergovernmental Panel on Climate Change (IPCC-AR5). In this manuscript, we focus on evaluating the ocean and land carbon cycle components of the NorESM, based on the control and historical simulations. Many of the observed large scale ocean biogeochemical features are reproduced satisfactorily by the NorESM. When compared to the climatological estimates from the World Ocean Atlas (WOA), the model simulated temperature, salinity, oxygen, and phosphate distributions agree reasonably well in both the surface layer and deep water structure. However, the model simulates a relatively strong overturning circulation strength that leads to noticeable model-data bias, especially within the North Atlantic Deep Water (NADW). This strong overturning circulation slightly distorts the structure of the biogeochemical tracers at depth. Advancements in simulating the oceanic mixed layer depth with respect to the previous generation model particularly improve the surface tracer distribution as well as the upper ocean biogeochemical processes, particularly in the Southern Ocean. Consequently, near surface ocean processes such as biological production and air-sea gas exchange, are in good agreement with climatological observations. NorESM reproduces the general pattern of land-vegetation gross primary productivity (GPP) when compared to the observationally-based values derived from the FLUXNET network of eddy covariance towers. Globally, the NorESM simulated annual mean GPP and terrestrial respiration are 129.8 and 106.6 Pg C yr^{-1}, slightly larger than observed of 119.4$\pm$5.9 and 96.4$\pm$6.0 Pg C yr^{-1}. The latitudinal distribution of GPP fluxes simulated by NorESM shows a GPP overestimation of 10% in the tropics and a substantial underestimation of GPP at high latitudes.

1 Introduction

In addition to the atmospheric radiative properties, global climate dynamics also depend on the complex simultaneous interactions between the atmosphere, ocean, and land. These interac-

tions are not only non-linear, but also introduce feedbacks of different magnitude and signs to the climate system. In order to understand the sophisticated interplay between the different components, Earth system models have been developed by the geoscientific community in recent years. The last Intergovernmental Panel for Climate Change Assessment Report (IPCC-AR4) stated that in order to produce a reliable future climate projection, such models are required (Denman et al., 2007).

An Earth system model typically consists of a global physical climate model coupled with land and ocean biogeochemical models (Bretherton, 1985), but can be extended to include further processes and reservoirs (e.g., anthropogenic interactions). As an integrated global model system, such model does not only simulate the change in climate physical variability due to anthropogenic drivers, but also includes climate feedbacks associated with the global carbon cycle. These feedback processes include changes in terrestrial and oceanic carbon uptake due to anthropogenic CO_2 emissions, perturbed surface temperature, precipitation, ocean circulation, sea-ice extent, biological productivity, etc. A new Norwegian Earth System Model (NorESM) was recently developed (Bentsen et al., submitted). The NorESM is among the many models used worldwide to project future climate change and is used for the coming IPCC-AR5. The ocean carbon cycle model in NorESM is unique compared to most other models due to its coupling with an isopycnic ocean model. Compared to the previous generation Bergen Earth system model (BCM-C, Tjiputra et al., 2010), the NorESM adopts new atmospheric, land, and sea-ice models, which are based on the Community Climate System Model (CCSM4, Gent et al., 2011). In addition, the ocean model resolution and mixing parameterization have been improved as well.

In this manuscript, we focus on evaluating the ocean and land carbon cycle components of the NorESM. In order to assess the quality of model projections, it is necessary to evaluate respective model simulations against the available present day climate and biogeochemical states. The biogeochemical states simulated by an Earth system model strongly depend on the quality of the physical fields in the model. Therefore, we will first analyze statistically how well the model simulates the climatological states of sea surface temperature and salinity. Next, the model simulated mean state of ocean biogeochemical tracers, such as oxygen, phosphate, and air-sea

3

CO$_2$ gas exchange are compared with the observations from the World Ocean Atlas (WOA) and other observational-based estimates. Finally, we will compare the land vegetation productivity and respiration simulated by NorESM with the observationally-based values derived from the FLUXNET network of eddy covariance towers.

The model description is presented in section 2. Section 3 describes the model experiment set up. The results of the experiment are discussed in section 4. Finally, conclusions are summarized in section 5.

2   Model description

The Norwegian Earth System Model (NorESM) is partly based on the recently released Community Climate System Model (CCSM4, Gent et al., 2011), which is maintained by the National Center for Atmospheric Research and is developed in partnership with collaborators funded primarily by the US National Science Foundation and the Department of Energy. It adopts the original coupler (CPL7), as well as terrestrial (CLM4, Lawrence et al., 2011), and sea ice (CICE4, Holland et al., 2012) components from CCSM4. The chemistry package in the atmospheric model (CAM4, Neale et al., submitted) is improved following Seland et al. (2008). In this section, we briefly describe the atmospheric, ocean, and land components of the NorESM. Since the physical components are documented in more detail by Bentsen et al. (submitted), here, major emphasis is placed on the carbon cycle components.

2.1   Atmospheric model

The atmospheric component in NorESM (CAM4-Oslo) is a modified version of the NCAR Community Atmospheric Model. The reader is referred to a manuscript by Neale et al. (submitted) for the original CAM4 model description. The difference from the original CAM4 model is the improvement in the aerosol and aerosol-cloud interactions as discussed in Seland et al. (2008) and Kirkevåg et al. (2008). For example, CAM4-Oslo includes tropospheric oxidants (e.g., OH, O$_3$, and H$_2$O$_2$) and a replenishment time which increases with the cloud volume

4

fraction. The ratio of organic matter to organic carbon aerosols related to the biomass burning primary organic matter emissions has been updated following Formenti et al. (2003). The prescribed AeroCom (Aerosol Comparisons project) sea salt emissions are replaced by prognostic (wind and temperature dependent) emissions (Struthers et al., 2011). The relative humidity threshold for formation of low clouds is reduced to 90%, and the critical droplet volume radius for onset of auro-conversion is increased to 14μm. A more recent and detailed description of CAM4-Oslo model will be available in Kirkevåg et al. (in preparation).

2.2 Ocean component

2.2.1 Ocean general circulation model

The ocean physical component of NorESM originates from the Miami Isopycnic Coordinate Ocean Model (MICOM; Bleck and Smith, 1990; Bleck et al., 1992) but with modified numerics and physics as described in Bentsen et al. (submitted). The main benefits of this version of model is accurate mixing and transport along isopycnic surfaces and good control on the diapycnal mixing that facilitates preservation of water masses during long model integrations. The vertical coordinate is potential density with reference pressure at 2000 dbar and provides reasonable neutrality of model layers in large regions of the ocean (McDougall and Jackett, 2005). The incremental remapping algorithm (Dukowicz and Baumgardner, 2000) is used for transport of layer thickness and tracers. The robust, accurate and efficient handling of numerous biogeochemical tracers was an important reason for selecting this transport algorithm. In Assmann et al. (2010) the analysis of biogeochemical tracers of Hamburg Oceanic Carbon Cycle (HAMOCC) model in an earlier version of this ocean model contributed to revealing issues in the representation of the Southern Ocean. Several of the later developments of the dynamical core and physical parameterizations was targeted to resolve some of these deficiencies. This includes changes in the treatment of near surface stability, modified parameterization of thickness and isopycnal eddy diffusivity, a different parameterization of mixed layer depth, and distribution of salt rejected during sea-ice freezing below the mixed layer. The model is configured on a grid with 1.125 degree horizontal resolution along the equator with grid singularities over

5

Antarctica and Greenland. The model has 53 vertical layers of which two are located in the surface mixed layer.

2.2.2 Ocean carbon cycle model

The NorESM employs the Hamburg Oceanic Carbon Cycle (HAMOCC5) model, which is based on the original work of Maier-Reimer (1993) and subsequent refinements (Maier-Reimer et al., 2005). It was recently coupled with the isopycnic MICOM model by Assmann et al. (2010). The HAMOCC5 model is embedded into the MICOM as a module, and hence has the same spatial resolution. Different from the earlier version (Tjiputra et al., 2010), the topmost mixed layer is divided into two layers, the uppermost of approximately 10 m depth, followed by a second layer representing the remainder of the mixed layer. The single 10 m layer improves the simulation of the surface ocean response to the atmospheric forcing (e.g., with respect to air–sea heat flux), which has been shown to also improve further process representations such as those of sea-ice formation.

The current version of the HAMOCC5 model includes a revised inorganic seawater carbon chemistry following the Ocean Carbon-cycle Model Intercomparison Project (OCMIP) protocols. The oceanic partial pressure of CO_2 (pCO_2) in the model is prognostically computed as a function of temperature, salinity, dissolved inorganic carbon (DIC), total alkalinity (TALK), and pressure. The HAMOCC5 simulates more than 30 biogeochemical tracers, which are advected by the circulation fields from MICOM. The model also includes a 12-layers sediment model, which is primarily relevant for long-term simulations ($>$1000 years).

HAMOCC5 employs an NPZD-type ecosystem model, initially implemented by Six and Maier-Reimer (1996). The nutrient compartment is represented by three macronutrients (phosphate, nitrate, and silicate), and one micronutrient (dissolved iron). The phytoplankton growth rate is formulated as a function of temperature and light availability according to Smith (1936) and Eppley (1972). In addition, phytoplankton growth is also co-limited by availability of phosphate, nitrate, and dissolved iron. Climatology monthly aerial iron deposition based on Mahowald et al. (2005) is applied in all model simulations. A fraction of the iron deposition (3.5%) is assumed to be immediately dissolved, where a fraction of it is immediately available

for biological production. In nitrate-limited oligotrophic regions, the model assumes nitrogen fixation by cyanobacteria, which is parameterized as the relaxation of the nitrate concentration at surface layer to the available phosphate concentration (by Redfield N:P ratio). Phytoplankton loss is modelled by specific mortality and exudation rates as well as zooplankton consumption. The dissolved organic carbon (DOC) produced by phytoplankton and zooplankton is freely advected by the ocean circulation and is remineralized at a constant rate. The parameterizations of the growth, grazing, and remineralization rates in the ecosystem module adopt a constant Redfield ratio to regulate the flow of carbon, oxygen, and nutrients between the different compartments.

The particles produced within the euphotic zone (i.e., 100m) depth are freely advected by the ocean circulation and exported with a prescribed vertical sinking speed. Particulate organic carbon (POC) associated with dead phytoplankton and zooplankton is transported vertically at 5 m day^{-1}. As POC sinks vertically, it is remineralized at a constant rate of 0.02 day^{-1}. Particulate inorganic matter calcium carbonate (PIC) and opal shells (biogenic silica) sink by 30 and 60 m day^{-1}, respectively. The distribution of calcium carbonate and biogenic silica export is formulated as a function of rain ratio and silicic acid concentration (Heinze, 2004). In general, when the silicic acid concentration is high, the export of biogenic silica increases and export of calcium carbonate decreases. Once exported out of the euphotic layer, biogenic silica is decomposed at depth with a constant redissolution rate constant. The calcium carbonate shells only dissolves when the simulated carbonate ion is less than the saturation state (i.e., CO_{3SAT}^{-2}) with a dissolvable maximum of 5% of calcium carbonate per time step. The non-remineralized particulate materials, reaching the sea floor sediment, undergo chemical reactions with the sediment pore waters, bioturbation and vertical advection within the sediment. Note that the current version of the model does not take into account influx of carbon and nutrients from the continental rivers, though lateral inflows from rivers can be activated.

The exchange of oxygen and CO_2 between the atmosphere and the surface ocean is simulated according to the Wanninkhof (1992) formulation. In principle, the air-sea gas exchange is determined by three components: the gas solubility in seawater, the gas transfer rate, and the gradient of the gas partial pressure between the atmosphere and the ocean surface. The solu-

bility of O_2 and CO_2 gases in seawater are derived as functions of surface ocean temperature and salinity following Weiss (1970, 1974). The gas transfer rate is computed as a function of Schmidt number and proportional to the square of surface wind speed. The model assumes that gas exchange occurs in ice-free regions only.

2.3   Land model

The NorESM adopts the Community Land Model version 4 (CLM4), which is the latest off-spring of the CLM family (Lawrence et al., 2012a). An extensive description of the model can be found at the website http://www.cesm.ucar.edu/models/ccsm4.0/clm/, as well as in the literature (Oleson et al., 2010; Lawrence et al., 2011). Only a brief overview of the model functionalities will be given in this manuscript.

The CLM4 integrates ecosystem cycling on the continental surface of water, energy, chemical elements, and trace gases. Spatial land surface heterogeneity is represented in a sub-grid cell hierarchy of multiple land units, columns, and plant functional types (PFTs). The land unit captures large-scale patterns of the landscape in the form of glaciers, lakes, wetlands, cities, and vegetated areas. The column level is used to represent the potential variability in the soil and snow state variables within a single land unit. The exchanges between the land surface and the atmosphere are defined at the PFT level. The vegetation state variables as well as the treatment for bare ground are computed at the PFT level. Sub-grid entities (land unit, column, and PFT) are independent from each other and maintain their own prognostic variables. All sub-grid units within a grid cell experience the same atmospheric forcing. In each grid-cell, sub-grid outputs are averaged and weighted by their fractional areas before they are transferred to the atmospheric model. A uniform soil type is maintained throughout one grid cell. Thermal and hydrologic properties of the soil depend on its texture (Clapp and Hornberger, 1978) and on its organic matter content (Lawrence et al., 2008). The soil profile is represented down to 50 meters. The 10 upper layers are hydrologically active (0 to 3.8 meters) while the five bedrock layers (below 3.8 m) act as a thermal reservoir.

Biogeophysical processes simulated by CLM4 include solar and longwave radiation interactions with vegetation canopy and soil, momentum and turbulent fluxes from canopy and soil,

heat transfer in soil and snow, hydrology of canopy, soil, and snow, and stomatal physiology as well as photosynthesis. The hydrology scheme in CLM4 includes the representation of water fluxes and reservoirs in snow layers, canopies, soils (including soil ice) and in an unconfined aquifer, as well as in glaciers, lakes, and rivers. The hydrology scheme uses the Richards equation following Zeng and Decker (2009). The soil water equations are solved for the top 10 layers of the profile. For each soil layer, the scheme simulates water transport taking into account infiltration, surface and sub-surface runoff, gradient diffusion, gravity, canopy transpiration through root extraction, and interactions with groundwater. An unconfined aquifer is added to the bottom of the soil column. Surface runoff in the model consists of overland flow due to saturation excess and infiltration excess. The saturated fraction of the soil column is a function of the water content, the fraction of surface layers being frozen (Niu and Yang, 2006), and the topography. The snow is represented by up to five snow layers. The snow parameterizations are primarily based on Dai and Zeng (1997). Snow evolution includes three types of processes: metamorphism, load compaction, and melting. The snow model in CLM4 includes new parameterizations for aerosol black carbon and dust deposition, grain-size dependent snow aging, vertically resolved snowpack heating (Flanner et al., 2007), snow cover fraction (Niu and Yang, 2006), and burial of short vegetation fraction (Wang and Zeng, 2009).

The carbon-nitrogen (CN) cycle model represents the biogeochemistry of carbon and nitrogen in vegetation, litter and soil-organic matter (Thornton et al., 2007). The assimilated carbon is estimated from photosynthesis. The amount of nitrogen available for plants is the sum of the nitrogen uptake in the soil and the re-translocation of nitrogen from senescing tissues. The nitrogen limitation acts on the gross primary production (GPP). A potential GPP is calculated from leaf photosynthetic rate without nitrogen constraint. The model diagnoses the needs of nitrogen to achieve this potential GPP, and accordingly, the actual GPP is decreased for nitrogen limitation. Inputs and losses of mineral nitrogen are taken into account in the form of nitrogen-atmospheric deposition, biological nitrogen fixation, denitrification, leaching, and losses in fire. A prognostic phenology scheme controls transfers of stored carbon and nitrogen out of storage pools for new tissues growth and losses of plant tissues to litter pools. Leaf and stem area indices for each plant functional type are derived from satellite data following the Lawrence et

al. (2011) methodology is prognostic. The spatial distribution of PFTs is updated on an annual time step. Transient land cover and land use change datasets used in CLM4 (Lawrence et al., 2012b) are derived from a global historical transient land use and land cover change data set (LUHa.v1) covering the period 1850-2005 (Hurtt et al., 2006).

3 Experiment design

Prior to any experiments, the NorESM model as a coupled system is spun up for 900 years. During this spin up we fixed the atmospheric CO_2 concentration at 284.7 ppm. For the spin up, the oceanic tracer fields were initialized as follows: the initial fields of oxygen and nutrients are derived from the World Ocean Atlas (WOA) (Garcia et al., 2010a,b). The dissolved inorganic carbon (DIC) and alkalinity fields are taken from the Global Data Analysis Project (GLODAP) dataset (Key et al., 2004). We use the $1°x1°$ gridded annual data of both data sets. Since the initialization is followed by a 900 year spin up, no special care was taken to conserve mass of the WOA and GLODAP fields. Rather, for each model grid cell, the closest data point is sought and a $10°x10°$ average around this point is assigned to the respective model grid cell. If no data is available at the location of a model grid cell (e.g. GLODAP provides no data in the Arctic ocean), a mean regional or a mean global profile is used there. The other biogeochemical variables in the water column (e.g., phytoplankton, zooplankton, dissolved organic carbon, etc.) and sediment compartments are initialized to zero or small but nonzero values. The spin up is important, particularly for the oceanic carbon cycle tracers to reach distributions which are reasonably close to equilibrium states. After approximately 500 model years, the simulated mean global surface air temperature reached an equilibrium mean state of approximately 13.6°C. In the coupled spin up, the CLM4 component uses land cover change data set (LUHa.v1, Hurtt et al. (2006)) of the first simulation year, 1850, as initial condition. CLM4 then runs from this initial state using the accelerated decomposition spin up mode (Thornton and Rosenbloom, 2005) for 600 simulation years.

Following the spin up, we performed two branch simulations, a control (CTRL) and a historical (HIST). For the CTRL simulation, we essentially extended the spin up for another 250

years (1850–2100). Here the non-evolving, preindustrial atmospheric aerosols and CO_2 concentration following the CMIP5 protocols are prescribed in the simulation. In addition, there is no anthropogenic land-use change applied in the CTRL. For the HIST simulation, the model is simulated for 156 years, representing the historical period from year 1850 to 2005. In the HIST simulation, observed changes in climate parameters are prescribed. These parameters include evolving atmospheric CO_2 concentration, anthropogenic aerosols and natural aerosols related to historical volcanic eruptions, as well as time-varying solar forcing. In addition, changes in land-use due to human activity are included in the HIST simulation. Note that both the CTRL and HIST simulations are performed with prescribed atmospheric CO_2 concentrations, and not with prescribed CO_2 emissions. The above conditions are applied according to the CMIP5 experimental design, documented by Taylor et al. (2012).

4 Results

4.1 Transient global temperature

The transient response of the global surface temperature simulated in the HIST period agrees reasonably well with observations. At the end of the HIST simulation (i.e., yr 2006), the global mean 2-m temperature has increased by approximately 0.9°C, whilst the SST has increased by 0.6°C relative to the year 1850. Figure 1 shows the evolution of global mean surface temperature anomaly (relative to 1961-1990 period) simulated by the NorESM together with observational based estimates from the Hadley Climate Research Unit (HadCRUT3, Brohan et al., 2006). The amplitude of the simulated multi-decadal variability throughout the historical period is in line with the observations. Following the 1991 mount Pinatubo eruption, the model simulates stronger cooling followed by stronger warming toward the end of the simulation.

4.2 Ocean biogeochemistry

Realistic simulation of the ocean biogeochemistry depends strongly on the background physical processes (Doney et al., 2004). Thus, in addition to different biogeochemical fields, we also

assess the model ability in simulating relevant physical fields, such as the temperature, salinity, and mixed layer depth. For observational-based climatology estimates, such as temperature, salinity, oxygen, or phosphate, we compare the HIST simulation over 1980-1999 period. For other observations such as DIC, ALK, and air-sea CO_2 fluxes, which are available in larger amounts only in more recent times, we compare them with the averaged model output over the 1996-2005 from the HIST simulation. Figure 2 shows the statistical summary of the simulated temperature and salinity as well as key biogeochemical tracers distribution when compared to the observation in form of a Taylor diagram (Taylor, 2001).

Compared to the WOA estimates (Locarnini et al., 2010), the model simulates realistically the mean annual surface temperature, in terms of amplitude and spatial distribution, as shown in Fig. 3. The Taylor diagram in Fig. 2 confirms very good model-data fit for surface temperature with correlation close to one. At depth, the vertical temperature structure in the Pacific is comparable with the observation. However, in the Atlantic section, the deep water temperature is noticeably warmer than the observation. The bias in the horizontal temperature distribution also increases from surface to deeper layers, as shown in Fig. 2. The relatively high Atlantic deep water temperature is partly attributed to the anomalously strong Atlantic Meridional Overturning Circulation (AMOC) strength in our present simulation. Here, the NorESM yields a relatively strong mean AMOC strength of 32 Sv compared to the observed estimates of 15.75±1.6 Sv (Ganachaud and Wunsch, 2000; Lumpkin and Speer, 2003).

The spatial distribution of the salinity field in NorESM broadly agrees with observations (Antonov et al., 2010) with noticeable differences, as shown in Fig. 4. At the surface, the model generally simulates lower salinity throughout most of the Southern Hemisphere subtropical gyres. In the Arctic, the model overestimates the surface salinity considerably by as much as 3 psu. The model-data difference in the Atlantic meridional section indicates that the model's deep and bottom water masses are generally somewhat too saline. In the North Atlantic, this is consistent with the strong AMOC of the model, as salinity changes dominate sea water density increases at low temperatures (occurring in high latitude regions with vertical convection due to hydrostatic instability). Around the 30°N latitude, the model simulates anomalously high deep-water salinities, which is attributed to a combination of too much outflow of saline water

from the Mediterranean Sea and relatively strong near surface mixing. This caveat is difficult to resolve with the current model horizontal resolution of approximately $1°$ since the width of Gibraltar Strait is roughly 30 km. The structure of Antarctic Intermediate Water (AAIW) and Sub-Antarctic Mode Water (SAMW) from the Southern Ocean is realistically simulated by the model, though the salinity in this feature is rendered as slightly too low.

Accurate representation of spatial and temporal mixed layer depth (MLD) is essential for many ocean biogeochemical processes. For example, winter mixing entrains DIC- and nutrient-rich deep water into the surface, which plays an important role in air-sea CO_2 fluxes and spring bloom biological production. Maps of mean mixed layer depth for the boreal winter (DJF) and summer (JJA) periods are shown in Fig. 5 together with observational-based estimates using a 0.2 degree temperature criterion (de Boyer Montégut et al., 2004). Regions with strong mixing simulated by the model generally correspond well with those observed. While the model still overestimates the mean MLD for the winter season in both hemispheres, it is substantially improved compared to the previous generation model (Tjiputra et al., 2010). In the Southern Ocean, improvement in mixed layer depth translates into a better simulated seasonal sea-air CO_2 gas exchange and biological production (see below).

4.2.1 Biogeochemical tracers

The dissolved inorganic nutrients are useful for assessing how well the model simulates the marine productivity, respiration, and remineralization of organic matter as well as the large scale ocean circulation. The large-scale spatial variation of mean surface phosphate concentration simulated by the NorESM is strongly correlated to the WOA estimate (Garcia et al., 2010b), as shown in Figs. 2 and 6. Regions of strong mixing and upwelling (e.g., North Atlantic, North Pacific, and Southern Ocean) yield higher phosphate concentrations than the mid-latitude regions. At high latitudes, relatively high nutrient concentrations are associated with the strong upwelling during wintertime mixing, where due to the low light conditions, nutrients cannot be depleted until spring or summer. In the equatorial regions (Pacific and Atlantic), the upwelled nutrients are steadily consumed by biological production due to its suitable location, which is not limited by light or temperature as at high latitudes. Also at mid latitudes optimum growth

13

conditions (i.e., year-long sufficient light and temperature) contribute to steadily low surface nutrient concentrations. In the North Atlantic, the model simulated surface phosphate is slightly higher than observed, but is much improved compared to the nearly depleted surface phosphate in the previous model generation (Assmann et al., 2010). In the Southern Ocean, improvement of mixing processes in the MICOM also yields more realistic phosphate distributions now.

Figure 6 shows that the phosphate concentration in the Atlantic and Pacific bottom water-masses are underestimated by the model. We believe this is largely attributed to the simulated strong overturning circulation (by the model), which results in a relatively young deep water mass with weak accumulation of remineralized nutrients in the deep Atlantic and Pacific Oceans. In the low-resolution version of the model (i.e., NorESM-L), the simulated overturning circulation is much more reasonable at ∼18 Sv (Zhang et al., 2012). There, the age of the water mass in the bottom water mass of Pacific Ocean is much older and the simulated phosphate concentration at depth is also much closer to the observation.

The NorESM simulated distributions of other macronutrients (nitrate, silicic acid) reveal comparable features with respect to corresponding field observations as phosphate and, there-fore, are not discussed here in further detail. Since there is no nutrient input from the river runoff, the model simulates a small drift in the global budget of nutrients, mainly due to loss to the sediments. A river runoff parameterization has already been implemented, but will be switched on in a later version of NorESM.

Figure 7 shows the simulated surface and vertical structure of dissolved oxygen as compared to the observations from the WOA (Garcia et al., 2010a). Along the surface, the dissolved oxygen of the model agrees well with the observations, as indicated by the strong correlation and small model-data misfit in Fig. 2. The dissolved oxygen close to the surface is mostly determined through air-sea gas exchange processes and through oxygen release during phyto-plankton growth. As the oxygen gas has higher solubility in colder water, maximum dissolved oxygen concentrations are simulated in the cold sub-polar and polar regions, whereas warm low latitude regions maintain lower oxygen concentrations. Below the surface layer and at depth, the oxygen is utilized predominantly for remineralization of organic matter. Therefore the oxygen structure of the model at depth is approximately the opposite of those for nutrient

(e.g., phosphate) concentrations. Regions of oldest water masses such as deep equatorial Pacific and Atlantic as well as deep North Pacific contain minimum oxygen concentrations. Regions of younger water masses along the North Atlantic Deep Water (NADW) and Antarctic Mode Water (AAMW) have relatively high oxygen concentrations. As mentioned above, since the model has very strong overturning circulation strength, it is expected that the deep water oxygen concentration in the model is somewhat overestimated with respect to measurements, which is shown in most of the bottom water masses.

Figure 8 shows that the surface concentration of DIC and ALK simulated by the model broadly agree with the observation in terms of the spatial distribution. However, the absolute value is slightly higher (5–10%) than the observation counterpart. Simulating the correct alkalinity distribution is known to be a problematic task in global carbon cycle models (e.g., Séférian et al., 2012). Nevertheless, despite the fact that both DIC and ALK are higher than the observed values, the model still simulates a reasonable surface sea-to-air carbon exchange compare to the observation as discussed below. This is because the carbon flux between the air-sea interface depends on, among others, the chemical buffering capacity of gaseous CO_2 in seawater. The inverse of this buffer capacity is known as the Revelle Factor (Revelle and Suess, 1957). The seawater buffer capacity is linearly correlated to the carbonate ion concentration. Thus regions with high carbonate ion concentrations such as the warm low latitude have high buffer capacity (low Revelle Factor), while the low carbonate and cold high latitude regions have low buffer capacity. The carbonate ion concentration can be estimated by subtracting DIC from TALK concentration. Figure 8 also shows the ALK minus DIC values from both the model and GLODAP data. Here, the model value compares fairly well with the observations in spatial variation as well as magnitude.

4.2.2 Biological production

To evaluate the ecosystem dynamics in the surface layer, we compare the model simulated net primary production to remote sensing-based estimates from Behrenfeld and Falkowski (1997). Regions with large primary production are found in the coastal upwelling regions, equatorial Pacific, and the high latitude oceans, as shown in Fig. 9. In the high latitude Southern Ocean, the

15

biological production in the model remains relatively low despite high macronutrients supply (e.g., see Fig. 6). This region is well known as high-nutrient-low-chlorophyll (HNLC) region associated to the limited dissolved iron concentration required for phytoplankton growth. The model-data deviation is largest in the eastern equatorial Pacific and parts of the Southern Ocean. In these regions, the model generally simulates higher NPP than observed. Carr et al. (2006) show that this caveat is common among many biogeochemical models, which maybe associated to the peculiar characteristic of the HNLC regions, where globally-tuned ecosystem parameterizations in models are likely to fail due to lack of a full understanding of the steering processes.

To further analyze the relationship between net primary production and nutrient, we compute the mean phosphate concentration at different latitudinal bands and ocean basins, and plot them against the respective mean net primary production as shown in Fig. 10. Figure 10 identifies three dominant productivity domains. The first is the low nutrient, low productivity region, which is confined to low latitudes. However, the equatorial Pacific is an exception, where the surface nutrient concentration is relatively low but the biological production is high. The second domain is the northern hemisphere at high latitudes (i.e., North Atlantic and North Pacific), characterized by high biological production with moderate nutrient concentration. These are also regions of strong export production, hence strong biological pump. The third domain is the Southern Ocean with high surface nutrient concentration but relatively low biological production. As mentioned above, this is due to the limited aerial iron deposition, which is an essential micronutrient for primary production.

Using the current model set up, the CTRL simulation yields a global mean net primary production of 42.2 ± 0.8 Pg C yr^{-1}. This value is well within the large range of estimates from both remote sensing and global biogeochemical model of 30 to 70 Pg C yr^{-1} (Carr et al., 2006). Even though there is a small negative drift in the nutrient budget associated to the sediment burial, the simulated global net primary production remains stable for the 250 years of CTRL simulation. Further, the NorESM simulates global particulate inorganic and organic carbon (PIC and POC) exports of 0.5 ± 0.01 and 8.3 ± 0.18 Pg C yr^{-1}, respectively. Thus the simulated PIC-to-POC ratio is approximately 0.06, also well within the range of 0.06 ± 0.03 given by Sarmiento et al. (2002).

4.2.3 Sea-air CO$_2$ fluxes

Figure 11 shows the simulated (HIST) mean annual sea-to-air CO$_2$ fluxes for the 1996–2005 period together with observational-based estimates by Takahashi et al. (2009) for the same period. The model broadly agrees with the observations in term of spatial variation with strongest carbon source to the atmosphere in the equatorial Pacific and largest carbon sink in the North Atlantic and Nordic Seas. In the equatorial Indian Ocean, the model outgassing is noticeably weaker than the data estimate. The model-data discrepancies are also pronounced in the polar Southern Ocean (South of 60°S), a region of increasing interest but still remaining poorly observed. Here, the model suggests a dominant carbon sink, whereas the data show a combination of weak sources and sinks regions. The possibility of considerable Southern Ocean carbon uptake from the atmosphere has been documented by anthropogenic carbon determinations (Vázquez-Rodríguez et al., 2009).

Compared to the preindustrial control (CTRL) simulation (not shown), the biggest difference occurs in the North Atlantic where some mean outgassing regions are completely replaced by carbon uptake. Under the preindustrial atmospheric CO$_2$ boundary condition (i.e., 284.7 ppm), the NorESM also simulates more intense carbon outgassing in the equatorial Pacific upwelling as well as the Southern Ocean circumpolar upwelling zone. Therefore, we assume that these three regions will play key role in controlling the oceanic carbon fluxes as the climate evolves in the future. In the midlatitude regions, there are relatively small changes in the carbon fluxes.

The time-series of net oceanic carbon uptake simulated by the HIST and CTRL simulation is shown in Fig. 12. In the 250 years of CTRL simulation, the ocean continues to take up CO$_2$ at 0.18 ± 0.08 Pg C yr^{-1}. In the HIST simulation, the model uptake rate is closely linked to the prescribed atmospheric CO$_2$ concentration. The sharp increase in atmospheric CO$_2$ after year 1950 leads to consistently more intense oceanic carbon uptake. Figure 12 shows that the model uptake for the years 1980s and 1990s agrees with the estimates from the IPCC-AR4 estimates (Denman et al., 2007). For the present day estimate (centered at year 2000), the model simulates a net carbon sink of 2.38 ± 0.12 Pg C yr^{-1}, well within the observation based estimates of 2.0 ± 1.0 Pg C yr^{-1} (Takahashi et al., 2009).

17

4.3 Terrestrial biogeochemistry

The evaluation of the carbon cycle processes in CLM4 have been partly documented in several prior studies (e.g., Bonan and Levis, 2010; Bonan et al., 2011; Lawrence et al., 2012b). The coupling of CLM4 to the NorESM model, in general, does not introduce substantial changes in the overall character of the land simulation. In this subsection, we discuss the general features of the CLM4 when coupled to the NorESM framework. The terrestrial carbon uptake simulated over the historical period is shown in Fig. 12. Compared to the control simulation, the terrestrial carbon uptake steadily increases from year 1850 to 2006. However, the terrestrial carbon uptake, excluding the land use change, remains lower than the estimates from IPCC-AR4 (Denman et al., 2007) for the 1980s and 1990s mean uptake.

The mean vegetation and soil carbon budget simulated by NorESM over the 1982–2005 historical period are 551.28 and 537.38 Pg C, respectively. Figure 13 shows the distribution of total vegetation and soil carbon contents as simulated by the NorESM. The ecosystem carbon content follows the precipitation and temperature distribution. The simulated amounts of carbon stored in vegetation biomass is in the range of observed values of 466–654 Pg C (WBGU, 1988; de Fries et al., 1999). However, the amount of carbon stored as organic matter in the soil is well below Jobbágy and Jackson (2000) global estimates of 1502 Pg C for the first meter depth. NorESM simulates regional soil carbon stock, which is lower by a factor of 2 to 10 than the values proposed by Jobbágy and Jackson (2000). The mismatch is particularly substantial in the high latitudes where NorESM simulates less than 2 kg C m^{-2} in tundra covered regions as compared to the observed values of 18 kg C m^{-2}. The low soil carbon at high latitudes is likely attributed to the lack representation of anoxic soil carbon decomposition and mixing properties. In addition, the litter decomposition is too fast and the soil organic carbon pools is not built-up fast enough during model's spin-up and hence remains low over the simulation periods. Unrealistically low GPP across much of the Arctic is also contributing to the bias in Arctic soil carbon stocks.

Here, we also compare the gross primary productivity (GPP) and terrestrial ecosystem respiration (TER=autotrophic+heterotrophic respirations) simulated by NorESM with the observa-

tionally derived values. While we can assess the capability of NorESM to fix and emit carbon on land, it is important to note that the fluxes due to changes in land use and management as well as fire are not taken into account in this analysis. The NorESM simulated GPP and TER are compared to the respective values derived from the FLUXNET network of eddy covariance towers. Jung et al. (2011) upscaled the FLUXNET-site observations to the global scale by using the Model Tree Ensembles (MTE) machine learning technique. The upscaling procedure made use of remotely sensed estimates of the fraction of absorbed photosynthetically active radiation, climate, and land cover data. The resulting data set hereafter defined as FLUXNET-MTE provides, for the period January 1982 to December 2005, monthly values of GPP and TER, at $0.5°$ spatial resolution. For the purpose of this analysis, the FLUXNET-MTE values were calculated to produce global and zonal estimates of the monthly values. The zonal estimates are computed for four latitudes slices: high latitude north ($>60°$N), mid-latitude north ($60°–20°$N), tropics ($20°$N–$20°$S), and mid-latitude south ($20°$S–$60°$S).

Table 1 summarizes the model simulated annual GPP and TER for the different latitudinal domains as compared to the observation. For the 1982–2005 period, the model simulates global annual GPP of 129.8 Pg C yr^{-1}, slightly larger than the FLUXNET-MTE measurements of 119.4$\pm$5.9 Pg C yr^{-1}. Nevertheless, the model value is still within the range of estimate obtained by Beer et al. (2010) based on flux-tower measurements and remote sensing for the period 1998–2005 of 123.0$\pm$8.0 Pg C yr^{-1}. Except for the northern hemisphere high latitude, the model consistently simulates larger GPP than the FLUXNET-MTE estimates, as shown in Table 1. In the mid-latitude north, tropics, and mid-latitude south regions, the model overestimates the observed GPP by approximately 10%, 10% and 17%,respectively, while at high latitude, the model underestimates the observations by approximately 45%.

The regional differences between the model simulated and observed TER resemble the similar patterns with GPP, with model overestimation in all regions except for the high latitude region, as shown in Table 1. Globally, the mean annual autotrophic and heterotrophic respiration simulated by NorESM are 83.2 and 23.4 Pg C yr^{-1}, respectively. In total, the simulated TER is 106.6 Pg C yr^{-1}, larger than estimates by Jung et al. (2011) of 96.4$\pm$6 Pg C yr^{-1}. Nevertheless, the simulated net ecosystem exchange (NEE), which can be estimated by subtracting

19

TER from GPP, is 23.2 Pg C yr^{-1} and remains within the range of values estimated by Jung et al. (2011). The model simulated spatial distribution of TER is similar to the GPP distribution. NorESM overestimates TER fluxes by 14.3% and 20.5% in the northern and southern mid-latitudes respectively when compared to the measurements. In the Tropics, simulated TER fluxes are 17.6% higher compared to the FLUXNET-MTE estimates, whereas at high latitudes, NorESM underestimates the observed TER by 31%.

Figure 14 shows the distribution of mean annual GPP fields simulated by NorESM and as estimated from FLUXNET-MTE. In general, the NorESM land carbon model overestimates the annual GPP compared to the FLUXNET-MTE in the tropics and throughout the extra-tropics. NorESM simulates more than 4 kg C m^{-2} GPP throughout regions covered with tropical rain forest. The NorESM overestimates the latitudinal distribution of GPP in the tropics and in the mid latitudes by approximately 15%. Such a pattern has been shown by Beer et al. (2010) to be produced by process-based models and more specifically by Bonan et al. (2011) for CLM4.0. The relatively large underestimation of GPP in the high latitudes might be due to the excessive nitrogen limitation and issue with cold region hydrology, which are currently being addressed for the version of CLM. Although this GPP discrepancy is locally quite strong, it represents only a small part in the total amount of carbon absorbed by land. Figure 15 shows the spatial TER distribution from NorESM and observations. The latitudinal patterns of TER follow very closely those shown by GPP due to the coupling existing between the two variables. First, a direct coupling where GPP provides substrate for the autotrophic respiration and secondly, a more loose coupling where GPP conditions the amount of carbon returning to the soil, which also determines the heterotrophic respiration.

Time-series of monthly GPP from the model and observations are shown in Fig. 16. Generally, the seasonal cycle is correctly simulated by the NorESM, with large productivity during respected hemispheres' summer season and low productivity in winter. In the northern hemisphere high latitude, the model simulated mean GPP is close to the observations, while the summer GPP is noticeable smaller than the observations. Here, we attribute the model-data discrepancies potentially to the temperature bias simulated by NorESM. During the summer months (June-July-August) in regions north of 60°N, the model simulated surface air tempera-

20

ture (at 2m level) is lower by 1 to 5K than the Climate Research Unit (CRU, New et al., 1999; Mitchell et al., 2005) as well as the National Centers for Environmental Prediction (NCEP, Saha et al., 2010) estimates. As temperature is a limiting factor for vegetation growth in these regions, lower temperatures induce a shorter growing season, and hence an underestimation of productivity. However, a stand-alone CLM4 simulation forced with observed climate also simulates a similar high latitude GPP bias (Swenson et al., accepted). In their study, Swenson et al. (accepted) suggest that other factors such as excessive nitrogen limitation and limitation associated with cold region soil hydrology may also play a role. In both hemispheres' mid-latitude regions, the model simulates reasonably well the amplitude and seasonal variability of GPP. In the tropics, the model GPP seasonal variation is comparable with the observation, but the model mean is considerably larger than the observations, by approximately 0.6 Pg C month^{-1}. With regards to long-term regional change in GPP, both model and observations suggest a relatively small positive trend, except for the mid-latitude southern region, where the trend is statistically no different than zero. Globally, the model suggests an increasing trend of 1.74 Tg C month^{-2}, more than three times larger than implied from the FLUXNET-MTE observation of 0.52 Tg C month^{-2}. We also note that there are uncertainties in the FLUXNET-MTE estimates associated with random and systematic errors from the upscaling methodology biases (Jung et al., 2011).

5 Summary and conclusions

In this manuscript, we evaluate the carbon cycle components of the Norwegian Earth System Model (NorESM). The NorESM model was developed based on several components of the Community Climate System Model (CCSM4). It keeps the original coupler (CPL7), terrestrial (CLM4), and sea ice (CICE4) components while the chemistry processes in the atmospheric model (CAM4) are improved. The ocean general circulation and carbon cycle models are replaced with the Miami Isopycnic Coordinate Ocean Model (MICOM) and the Hamburg Oceanic Carbon Cycle (HAMOCC) model. In addition to control and historical simulations as discussed, the NorESM also performed many other simulations to support the coming Fifth Assessment Report of the Intergovernmental Panel on Climate Change (IPCC-AR5). The NorESM model

output is available for download at the CMIP5 (Coupled Model Intercomparison Project) website, http://cmip-pcmdi.llnl.gov/cmip5/.

The ocean carbon cycle model in NorESM is unique because of the coupling with an isopycnic ocean model. In general, the global distribution of temperature and salinity as well as biogeochemical tracers such as oxygen and nutrient agree broadly with climatological estimates from the World Ocean Atlas (WOA). The model performs especially well in simulating the observed large scale temperature amplitude and spatial variability. Surface distributions of oxygen and phosphate have been noticeably improved with respect to an earlier model version. This progress is attributed to the improved mixing parameterization in the recent MICOM model version. A relatively strong AMOC strength of ∼32 Sv leads to model-data bias particularly in the North Atlantic Deep Water masses.

The land carbon cycle model in NorESM is represented with the latest off-spring of the CLM family, CLM4. With this land module, the NorESM reproduces the general pattern of the vegetation carbon content. However, CLM4 in NorESM considerably underestimates the soil carbon content, which appears to be due to poorly or incompletely represented biogeochemical and hydrologic processes in CLM4 rather than due to biases in the coupled climate simulation. Compared to the FLUXNET-MTE measurements, the NorESM simulates the land-vegetation gross primary productivity reasonably well. Our analysis shows that the model simulates consistent amplitude and seasonal cycle as observed in mid-latitudes but considerable biases remain in the tropics and at high latitudes. The model-data disagreement in the tropics is due to excessive productivity, which has also been documented by Bonan et al. (2011). At high latitudes, the temperature bias, particularly in the summer months may be responsible for the model uncertainties. The future development effort will be oriented toward a better parameterization of the carbon absorption by vegetation as well as improved and more process based representation of the ecosystem respiration. Much efforts and methodological considerations will also be needed to improve the soil carbon content predictions.

The model will also be continuously developed to include land-ocean coupling by parameterizing the fluxes of carbon, nutrients, and dissolved oxygen into the continental margins through river-runoff. The parameterization will be based on observational data and formulated as a func-

22

tion of weathering, temperature, and precipitation similar to Bernard et al. (2011). We also plan to improve the nitrogen cycle in the ocean biogeochemistry model, focusing on the changes in marine N_2O sources and sinks to the atmosphere under present and future climate change.

References

Antonov, J. I., Seidov, D., Boyer, T. P., Locarnini, R. A., Mishonov, A. V., Garcia, H. E., Baranova, O. K., Zweng, M. M., and Johnson, D. R.: World Ocean Atlas 2009, Volume 2: Salinity, edited by Levitus, S., NOAA Atlas NESDIS 69, U.S. Government Printing Office, Washington, D.C., 184 pp., 2010.

Assmann, K. M., Bentsen, M., Segschneider, J., and Heinze, C.: An isopycnic ocean carbon cycle model, Geosci. Model Dev., 3, 143–167, 2010.

Beer, C., Reichstein, M., Tomelleri, E., Ciais, P., Jung, M., Carvalhais, N., Rödenbeck, C., Arain, M. A., Baldocchi, D., Bonan, G. A., Bondeau, A., Cescatti, A., Lasslop, G., Lindroth, A., Lomas, M., Luyssaert, S., Margolis, H., Oleson, K. W., Roupsard, O., Veenendaal, E., Viovy, N., Williams, C., Woodward, F. I., Papale, D.: Terrestrial gross carbon dioxide uptake: Global distribution and covariation with climate, Science, 329, 834–838, doi:10.1126/science.1184984, 2010.

Behrenfeld, M. J. and Falkowski, P. G.: Photosynthetic rates derived from satellite-based chlorophyll concentration, Limnol. Oceanogr., 42(1), 1–20, 1997.

Bentsen, M., Bethke, I., Debernard, J. B., Kirkevåg, A., Seland, Ø., Drange, H., Iversen, I., Roelandt, C., Seierstad, A., Hoose, C., and Kristjansson, J. E.: The Norwegian Earth System Model, NorESM1-M. Part 1: Description and basic evaluation, Geosci. Model Dev. Discuss., Submitted.

Bernard, C. Y., Dürr, H. H., Heinze, C., Segschneider, J., and Maier-Reimer, E.: Contribution of riverine nutrients to the silicon biogeochemistry of the global ocean – a model study, Biogeosciences, 8, 551–564, doi:10.5194/bg-8-551-2011, 2011.

Bleck, R. and Smith, L. T.: A wind-driven isopycnic coordinate model of the North and Equatorial Atlantic Ocean. 1. Model development and supporting experiments, J. Geophys. Res., 95, 3273–3285, 1990.

Bleck, R., Rooth, C., Hu, D., and Smith, L. T.: Salinity-driven Thermocline Transients in a Wind- and Thermohaline-forced Isopycnic Coordinate Model of the North Atlantic, J. Pys. Oceanogr., 22, 1486–1505, 1992.

Bonan, G. B. and Levis, S.: Quantifying carbon-nitrogen feedbacks in the community land model (CLM4), Geophys. Res. Lett., 37, L07401, doi:10.1029/2010GL042430, 2010.

Bonan, G. B., Lawrence, P. J., Oleson, K. W., Levis, S., Jung, M., Reichstein, M., Lawrence, D. M., and Swenson S. C.: Improving canopy processes in the Community Land Model version 4 (CLM4) using global flux fields empirically inferred from FLUXNET data, J. Geophys. Res., 116, G02014, doi:10.1029/2010JG001593, 2011.

Bretherton, F. P.: Earth system science and remote sensing, Proceedings of the IEEE, 73(6), 1118–1127, 1985.

Brohan, P., Kennedy, J. J., Harris, I., Tett, S. F. B., and Jones, P. D.: Uncertainty estimates in the regional and global observed temperature changes: A new data set from 1850, J. Geophys. Res., 111, D122106, doi:10.1029/2005JD006548, 2006.

Carr, M.-E., Friedrichs, M. A. M., Schmeltz, M., Aita, M. N., Antoine, D., Arrigo, K. R., Asanuma, I., Aumont, O., Barber, R., Behrenfeld, M., Bidigare, R., Buitenhuis, E. T., Campbell, J., Ciotti, A., Dierssen, H., Dowell, M., Dunne, J., Esaias, W., Gentili, B., Gregg, W., Groom, S., Hoepffner, N., Ishizaka, J., Kameda, T., Le Quéré, C., Lohrenz, S., Marra, J., Mélin, F., Moore, K., Morel, A., Reddy, T. E., Ryan, J., Scardi, M., Smyth, T., Turpie, K., Tilstone, G., Waters, K., and Yamanaka, Y.: A comparison of global estimates of marine primary production from ocean color, Deep-Sea Res. Pt. II, 53, 741770, doi:10.1016/j.dsr2.2006.01.028, 2006.

Clapp, R. B. and Hornberger, G. M.: Empirical equations for some soil hydraulic properties, Water Resour. Res., 14, 601–604, 1978.

Dai, Y. and Zeng, Q.: A land surface model (IAP94) for climate studies. Part I: formulation and validation in off-line experiments, Adv. Atmos. Sci., 14, 433–460, 1997.

de Boyer Montégut, C., Madec, G., Fischer, A. S., Lazar, A., and Iudicone, D.: Mixed layer depth over the global ocean: an examination of profile data and a profile-based climatology, J. Geophys. Res.,

109, C12003, doi:10.1029/2004JC002378, 2004.

De Fries, R. S., Field, C. B., Fung, I., Collatz, G. J., and Bounoua L.: Combining satellite data and biogeochemical models to estimate global effects of human-induced land cover change on carbon emissions and primary productivity, Global Biogeochemical Cycles, 13, 803–815, 1999.

Denman, K. L., Brasseur, G., Chidthaisong, A., Ciais, P., Cox, P. M., Dickinson, R. E., Hauglustaine, D., Heinze, C., Holland, E., Jacob, D., Lohmann, U., Ramachandran, S., da Silva Dias, P. L., Wofsy, S. C., and Zhang, X.: Couplings Between Changes in the Climate System and Biogeochemistry, in: Climate Change 2007: The Physical Science Basis, Contribution of Working Group I to the Fourth Assessment Report of the Intergovernmental Panel on Climate Change, edited by Solomon, S., Qin, D., Manning, M., Chen, Z., Marquis, M., Averyt, K. B., Tignor, M., and Miller, H. L., Cambridge University Press, Cambridge, United Kingdom and New York, NY, USA, 2007.

Doney, S. C., Lindsay, K., Caldeira, K., Campin, J.-M., Drange, H., Dutay, J.-C., Follows, M., Gao, Y., Gnanadesikan, A., Gruber, N., Ishida, A., Joos, F., Madec, G., Maier-Reimer, E., Marshall, J. C., Matear, R. J., Monfray, P., Mouchet, A., Najjar, R., Orr, J. C., Plattner, G.-K., Sarmiento, J., Schlitzer, R., Slater, R., Totterdell, I. J., Weirig, M.-F., Yamanaka, Y., and Tool, A.: Evaluating global ocean carbon models: The importance of realistic physics, Global Biogeochem. Cycles, 18, GB3017, doi:10.1029/2003GB002150, 2004.

Dukowicz, J. K. and Baumgardner, J. R.: Incremental remapping as a transport/advection algorithm, J. Comput. Phys., 160, 318-335, 2000.

Eppley, R. W.: Temperature and phytoplankton growth in the sea, Fish. Bull., 70, 1063–1085, 1972.

Flanner, M. G., Zender, C. S., Randerson, J. T., and Rasch, P. J.: Present day climate forcing and response from black carbon in snow, J. Geophys. Res., 112, D11202, doi:10.1029/2006JD008003, 2007.

Formenti, P., Elbert, W., Maenhaut, J., Haywood, S., Osborne, S., and Andreae, M. O.: Inorganic and carbonaceous aerosols during the Southern African Regional Science Initiative (SAFARI 2000) experiment: Chemical characteristics, physical properties, and emission data for smoke from African biomass burning, J. Geophys. Res., 108, 1–16, 2003.

Ganachaud, A. and Wunsch, C.: Improved estimates of global ocean circulation, heat transport and mixing from hydrographic data, Nature, 408, 453–457, 2000.

Garcia, H. E., Locarnini, R. A., Boyer, T. P., Antonov, J. I., Baranova, O. K., Zweng, M. M., and Johnson, D. R.: World Ocean Atlas 2009, Volume 3: Dissolved Oxygen, Apparent Oxygen Utilization, and Oxygen Saturation, edited by Levitus, S., NOAA Atlas NESDIS 70, U.S. Government Printing Office, Washington, D.C., 344 pp., 2010a.

Garcia, H. E., Locarnini, R. A., Boyer, T. P., Antonov, J. I., Zweng, M. M., Baranova, O. K., and Johnson,

D. R.: World Ocean Atlas 2009, Volume 4: Nutrients (phosphate, nitrate, silicate), edited by Levitus, S., NOAA Atlas NESDIS 71, U.S. Government Printing Office, Washington, D.C., 398 pp., 2010b.

Gent, P. R., Danabasoglu, G., Donner, L. J., Holland, M. M., Hunke, E. C., Jayne, S. R., Lawrence, D. M., Neale, R. B., Rasch, P. J., Vertenstein, M., Worley, P. H., Yang, Z. L., and Zhang, M.: The Community Climate System Model Version 4, J. CLimate, 24, 4973–4991, doi: http://dx.doi.org/10.1175/2011JCLI4083.1, 2011.

Heinze, C.: Simulating oceanic $CaCO_3$ export production in the greenhouse, Geophys. Res. Lett., 31, L16308, doi:10.1029/2004GL020613, 2004.

Holland, M. M., Bailey, D. A., Briegleb, B. P., Light, B., and Hunke, E.: Improved sea ice shortwave radiation physics in CCSM4: The impact of melt ponds and aerosols on Arctic Sea ice, J. Clim., doi:10.1175/JCLI-D-11-00078.1, 2012.

Hurtt, G. C., Frolking, S., Fearon, M. G., Moore, B., Shevliakova, E., Malyshev, S., Pacala, S. W., and Houghton, R. A.: The underpinnings of land-use history: three centuries of global gridded land-use transitions, wood-harvest activity, and resulting secondary lands, Glob. Change Biol., 12, 1208–1229, 2006.

Jobbágy, E. G. and Jackson, R. B.: The vertical distribution of soil organic carbon and its relation to climate and vegetation, Ecological Applications, 10(2), pp. 423–436, 2000.

Jung, M., Reichstein, M., Margolis, H. A., Cescatti, A., Richardson, A. D., Arain, M. A., Arneth, A., Bernhofer, C., Bonal, D., Chen, J., Gianelle, D., Gobron, N., Kiely, G., Kutsch, W., Lasslop, G., Law, B. E., Lindroth, A., Merbold, L., Montagnani, L., Moors, E. J., Papale, D., Sottocornola, M., Vaccari, F., and Williams, C.: Global patterns of land-atmosphere fluxes of carbon dioxide, latent heat, and sensible heat derived from eddy covariance, satellite, and meteorological observations, J. Geophys. Res., 116, G00J07, doi: 10.1029/2010JG001566, 2011.

Key, R. M., Kozyr, A., Sabine, C. L., Lee, K., Wanninkhof, R., Bullister, J. L., Feely, R. A., Millero, F. J., Mordy, C., and Peng, T.-H.: A global ocean carbon climatology: Results from Global Data Analysis Project (GLODAP), Global Biogeochem. Cy., 18, GB4031, doi:10.1029/2004GB002247, 2004.

Kirkevåg, A., Iversen, T., Seland, Ø., Debernard, J. B., Storelvmo, T., and Kristjánsson, J. E.: Aerosol–cloud–climate interactions in the climate model CAM–Oslo, Tellus, 60A, 492–512, 2008.

Kirkevåg, A., Iversen, T., Seland, Ø., Struthers, H., Hoose, C., and Nilsson, D.: Aerosols and their radiative effects on climate in CAM4-Oslo/NorESM. The importance of natural aerosols for estimates of anthropogenic impacts, In preparation, 2012.

Koeve, W.: Upper ocean carbon fluxes in the Atlantic Ocean: The importance of the POC:PIC ratio, Global Biogeochem. Cycles, 16(4), 1056, doi:10.1029/2001GB001836, 2002.

Lawrence, D. M., Slater, A. G., Romanovsky, V. E., and Nicolsky, D. J.: The sensitivity of a model projection of near-surface permafrost degradation to soil column depth and inclusion of soil organic matter, J. Geophys. Res., 113, F02011, doi:10.1029/2007JF000883, 2008.

Lawrence, D., Oleson, K. W., Flanner, M. G., Thornton, P. E., Swenson, S. C., Lawrence, P. J., Zeng, X., Yang, Z.-L., Levis, S., Skaguchi, K., Bonan, G. B., and Slater, A. G.: Parameterization improvements and functional structural advances in version 4 of the Community Land Model, J. Adv. Model. Earth Syst., 3, M03001, doi:10.1029/2011MS000045, 2011.

Lawrence, D. M., Oleson, K. W., Flanner, M. G., Fletcher, C. G., Lawrence, P. J., Levis, S., Swenson, S. C., and Bonan, G. B.: The CCSM4 land simulation, 1850–2005: Assessment of surface climate and new capabilities, J. Climate, oi:10.1175/JCLI-D-11-00103.1, 2012.

Lawrence, P. J., Feddema, J. J., Bonan, G. B., Meehl, G. A., O'Neill, B. C., Levis, S., Lawrence, D. M., Oleson, K. W., Kluzek, E., Lindsay, K., and Thornton, P. E.: Simulating the biogeochemical and biogeophysical impacts of transient land cover change and wood harvest in the Community Climate System Model (CCSM4) from 1850 to 2100, J. Climate CCSM4 Special Collection, 25, 3071-3095, doi:10.1175/JCLI-D-11-00256.1, 2012.

Locarnini, R. A., Mishonov, A. V., Antonov, J. I., Boyer, T. P., Garcia, H. E., Baranova, O. K., Zweng, M. M., and Johnson D. R.: World Ocean Atlas 2009, Volume 1: Temperature, edited by Levitus, S., NOAA Atlas NESDIS 68, U.S. Government Printing Office, Washington, D.C., 184 pp, 2010.

Lumpkin, R. and Speer, K.: Large-scale vertical and horizontal circulation in the North Atlantic Ocean, J. Phys. Oceanogr., 33, 1902–1920, 2003.

Mahowald, N., Baker, A., Bergametti, G., Brooks, N., Duce, R., Jickells, T., Kubilay, N., Prospero, J., and Tegen, I.: Atmospheric global dust cycle and iron inputs to the ocean, Global Biogeochem. Cy., 19(4), GB4025, doi:10.1029/2004GB002402, 2005.

Maier-Reimer, E.: Geochemical cycles in an ocean general circulation model, Preindustrial tracer distributions, Global Biogeochem. Cycles, 7, 645–677, 1993.

Maier-Reimer, E., Kriest, I., Segschneider, J., and Wetzel, P.: The HAMburg Ocean Carbon Cycle Model HAMOCC5.1 - Technical Description Release 1.1, Berichte zur Erdsystemforschung 14, ISSN 1614-1199, Max Planck Institute for Meteorology, Hamburg, Germany, 50pp, 2005.

McDougall, T. J. and Jackett, D. R.: An assessment of orthobaric density in the global ocean, J. Phys. Oceanogr., 35, 2054-2075, 2005.

Mitchell, T. D. and Jones P. D.: An improved method of constructing a database of monthly climate observations and associated high-resolution grids, Int. J. Climatol., 25, 693–712, doi:10.1002/joc.1181, 2005.

Neale, R. B., Richter, J., Park, S., Lauritzen, P. H., Vavrus, S. J., Rasch, P. J., and Zhang, M.: The mean climate of the Community Atmosphere Model (CAM4) in forced SST and fully coupled experiments, J. Climate, submitted.

New, M., Hulme, M. and Jones, P. D.: Representing twentieth century space-time climate variability. Part 1: development of a 1961-90 mean monthly terrestrial climatology, J. Climate, 12, 829–856, 1999.

Niu, G.-Y. and Yang, Z.-L.: Effects of frozen soil on snowmelt runoff and soil water storage at a continental scale, J. Hydrometeor, 7, 937–952, 2006.

Oleson, K. W., Lawrence, D. M., Bonan, G. B., Flanner, M. G., Kluzek, E., Lawrence, P. J., Levis, S., Swenson, S. C., Thornton, P. E., Dai, A., Decker, M., Dickinson, R., Feddema, J., Heald, C. L., Hoffman, F., Lamarque, J. F., Mahowald, N., Niu, G.-Y., Qian, T., Randerson, J., Running, S., Sakaguchi, K., Slater, A., Stockli, R., Wang, A., Yang, Z.-L., Zeng, X and X. Zeng: Technical description of version 4.0 of the Community Land Model, NCAR Tech. Note, NCAR/TN-478+STR, 257 pp, 2010.

Revelle, R. and Suess, H. E.: Carbon dioxide exchange between atmosphere and ocean and the question of atmospheric CO_2 during past decades, Tellus, 9, 18–27, 1957.

Saha, S., Moorthi, S., Pan, H.-L., Wu, X., Wang, J., Nadiga, S., Tripp, P., Kistler, R., Woollen, J., Behringer, D., Liu, H., Stokes, D., Grumbine, R., Gayno, G., Wang, J., Hou, Y.-T., Chuang, H., Juang, H.-M. H., Sela, J., Iredell, M., Treadon, R., Kleist, D., Delst, P. V., Keyser, D., Derber, J., Ek, M., Meng, J., Wei, H., Yang, R., Lord, S., van den Dool, H., Kumar, A., Wang, W., Long, C., Chelliah, M., Xue, Y., Huang, B., Schemm, J.-K., Ebisuzaki, W., Lin, R., Xie, P., Chen, M., Zhou, S., Higgins, W., Zou, C.-Z., Liu, Q., Chen, Y., Han, Y., Cucurull, L., Reynolds, R. W., Rutledge, G., and Goldberg, M.: The NCEP climate forecast system reanalysis, Bull. Amer. Meteor. Soc., 91, 1015–1057, doi:10.1175/2010Bams3001.1, 2010.

Sarmiento, J. L., Dunne, J., Gnanadesikan, A., Key, R. M., Matsumoto, K., and Slater, R.: A new estimate of the $CaCO_3$ to organic carbon export ratio, Global Biogeochem. Cycles, 16(4), 1107, doi:10.1029/2002GB001919, 2002.

Séférian, R., Bopp, L., Gehlen, M., Orr, J., Ethé, C., Cadule, P., Aumont, O., Salas-y-Mélia, D., Voldoire, A., and Madec, G.: Skill assessment of three Earth system models with common marine biogeochemistry, CLim. Dyn. doi:10.1007/s00382-012-1362-8, 2012.

Seland, Ø., Iversen, T., Kirkevåg, A., and Storelvmo, T.: Aerosol–climate interactions in the CAM-Oslo atmospheric GCM and investigation of associated basic shortcomings, Tellus, 60A, 459–491, 2008.

Six, K. D. and Maier-Reimer, E.: Effects of plankton dynamics on seasonal carbon fluxes in an ocean general circulation model, Global Biogeochem. Cy., 10, 559–583, 1996.

Smith, E. L.: Photosynthesis in relation to light and carbon dioxide, Proc. Natl. Acad. Sci. U.S.A., 22,

504–511, 1936

Struthers, H., Ekman, A. M. L., Glantz, P., Iversen, T., Kirkevåg, A., Mårtensson, E. M., Seland, Ø., and Nilsson, E. D.: The effect of sea ice loss on sea salt aerosol concentrations and the radiative balance of the Arctic, Atmos. Chem. Phys., 11, 3459–3477, 2011.

Swenson, S. C., Lawrence, D. M., and Lee, H.: Improved simulation of the terrestrial hydrological cycle in permafrost regions by the Community Land Model, J. Adv. Model. Earth Syst., accepted.

Takahashi, T., Sutherland, S. C., Wanninkhof, R., Sweeney, C., Feely, R. A., Chipman, D. W., Hales, B., Friedrich, G., Chavez, F., Sabine, C., Watson, A., Bakker, D. C. E., Schuster, U., Metzl, N., Yoshikawa-Inoue, H., Ishii, M., Midorikawa, T., Nojiri, Y., Körtzinger, A., Steinhoff, T., Hoppema, M., Olafsson, J., Arnarson, T. S., Tilbrook, B., Johannessen, T., Olsen, A., Bellerby, R., Wong, C. S., Delille, B., Bates, N. R., and de Baar, H. J. W.: Climatological mean and decadal change in surface ocean pCO_2, and net sea-air CO_2 flux over the global oceans, Deep-Sea Res. II, 56, 554–577, doi:10.1016/j.dsr2.2008.12.009, 2009.

Taylor, K. E.: Summarizing multiple aspects of model performance in a single diagram, J. Geophys. Res., 106, 7183-7192, 2001.

Taylor, K. E., Stouffer, R. J., and Meehl, G. A.: An Overview of CMIP5 and the experiment design, Bull. Amer. Meteor. Soc., 93, doi:10.1175/BAMS-D-11-00094.1, 2012.

Thornton, P. E., and Rosenbloom, N. A.: Ecosystem model spin-up: estimating steady state conditions in a coupled terrestrial carbon and nitrogen cycle model, Ecological Modelling, 189, 25–48, 2005.

Thornton, P. E., Lamarque, J.-F., Rosenbloom, N. A., and Mahowald, N. M.: Influence of carbon-nitrogen cycle coupling on land model response to CO2 fertilization and climate variability, Global Biogeochem. Cycles, 21, GB4018, 2007.

Tjiputra, J. F., Assmann, K., Bentsen, M., Bethke, I., Otterå, O. H., Sturm, C., and Heinze, C.: Bergen Earth system model (BCM-C): model description and regional climate-carbon cycle feedbacks assessment, Geosci. Model Dev., 3, 123–141, http://dx.doi.org/10.5194/gmd-3-123-2010doi:10.5194/gmd-3-123-2010, 2010.

Vázquez-Rodríguez, Touratier, M. F., Lo Monaco, C., Waugh, D. W., Padin, X. A., Bellerby, R. G. J., Goyet, C., Metzl, N., Ríos, A. F., and Pérez, F. F.: Anthropogenic carbon distribution in the Atlantic Ocean: data-based estimates from the Arctic to the Antarctic, Biogeosciences, 6, 439–451, 2009.

Wang, A. and Zeng, X.: Improving the treatment of vertical snow burial fraction over short vegetation in the NCAR CLM3, Adv. Atmos. Sci., 26, 877-886, doi:10.1007/s00376-009-8098-3, 2009.

Wanninkhof, R.: Relationship between wind speed and gas exchange over the ocean, J. Geophys. Res., 97, 7373-7382, 1992.
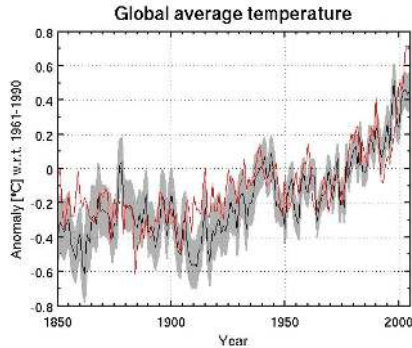
Fig. 1. Time series of model simulated global mean surface temperature anomaly with respect to the 1961–1990 period (red line). Plotted together is the observational estimate from the HadCRUT3 product (black line) with the respective uncertainty range in grey shades (Brohan et al., 2006).

WBGU (Wissenschaftlicher Beirat der Bundesregierung Globale Umweltveränerungen, Die Anrechnung biolischer Quellen und Senken in Kyoto-Protokoll: Fortschritt oder Rückschlang für den globalen Umweltschutz Sondergutachten 1988, Bremerhaven, Germany, 76pp, 1988.

Weiss, R. F.: The solubility of nitrogen, oxygen and argon in water and sea water, Deep-Sea Res., 17, 721-735, 1970.

Weiss, R. F.: Carbon dioxide in water and seawater: The solubility of a non-ideal gas, Mar. Chem., 2, 203-215, 1974.

Zeng, X., and Decker, M.: Improving the numerical solution of soil moisture-based Richards equation for land models with a deep or shallow water table, J. Hydrometeor. 10, 308–319, 2009.

Zhang, Z. S., Nisancioglu, K., Bentsen, M., Tjiputra, J., Bethke, I., Yan, Q., Risebrobakken, B., Andersson, C., and Jansen, E.: Pre–industrial and mid-Pliocene simulations with NorESM–L, Geosci. Model Dev. Discuss., 5, 119-148, doi:10.5194/gmdd-5-119-2012, 2012.
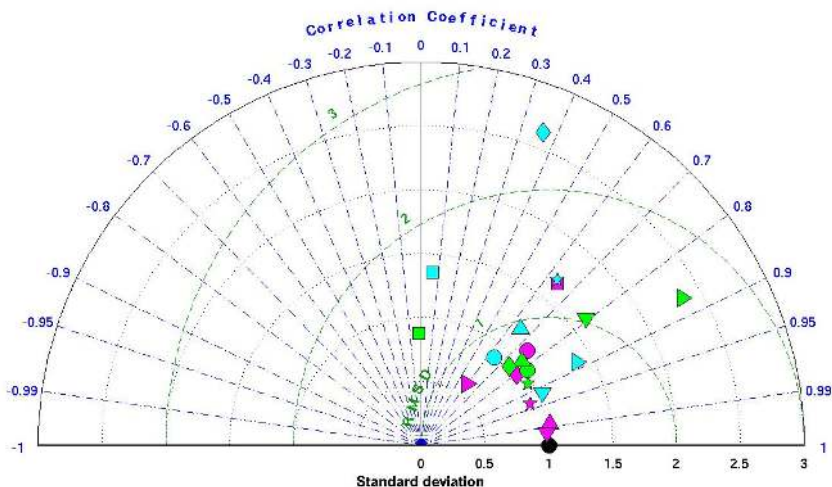
Fig. 2. Taylor diagram of non-area weighted statistical summary between the simulated and observed annually-averaged (climatology) of (▽) ocean temperature, (▷) salinity, (⋆) phosphate, (△) dissolved oxygen, (○) silicate, (◇) dissolved inorganic carbon, and (□) alkalinity. Shown here are comparison at surface (magenta), 1000 meter (blue), and 3000 meter (green) depths. Observations are based on the World Ocean Atlas (WOA) and GLODAP (see also text). The black circle represents the observations. All standard deviations are normalized to the respected observed standard deviation. For temperature, salinity, phosphate, silicate and oxygen, we compare the HIST simulation from 1980–1999 period, whereas for DIC and ALK, we use the 1996–2005 simulation period.
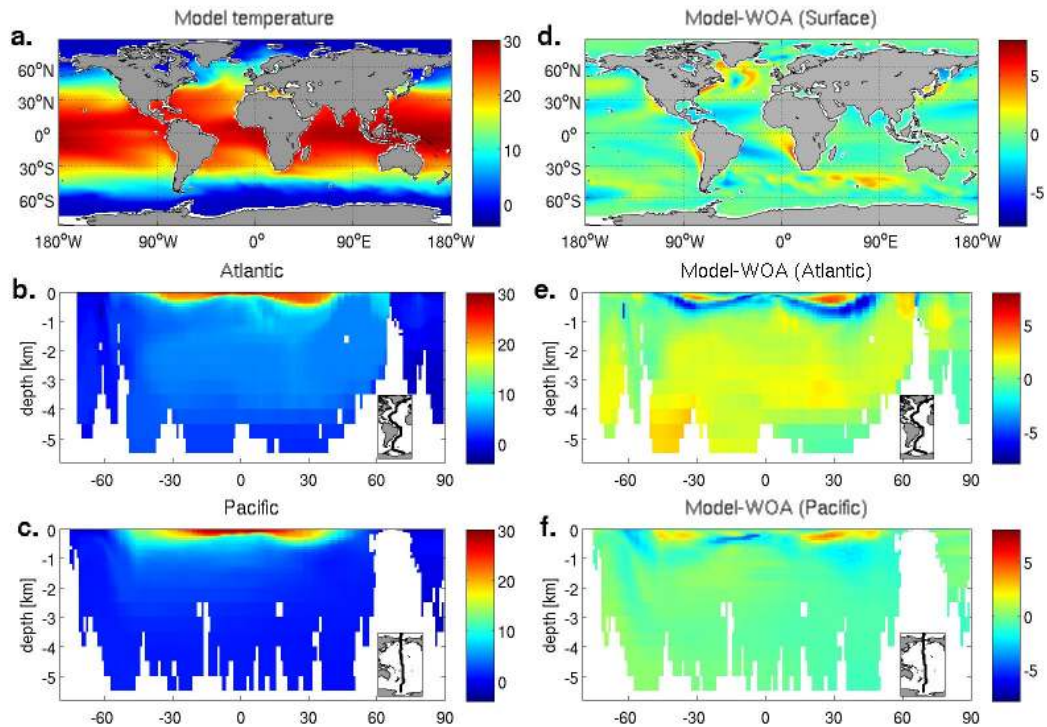
Fig. 3. Distribution of ocean temperature from model simulation (left) and difference in temperature between the model and climatological estimates (right) (WOA, Locarnini et al., 2010) for the surface (a,d), Atlantic (b,e) and Pacific (c,f) vertical sections. Units are in [degree C].

32
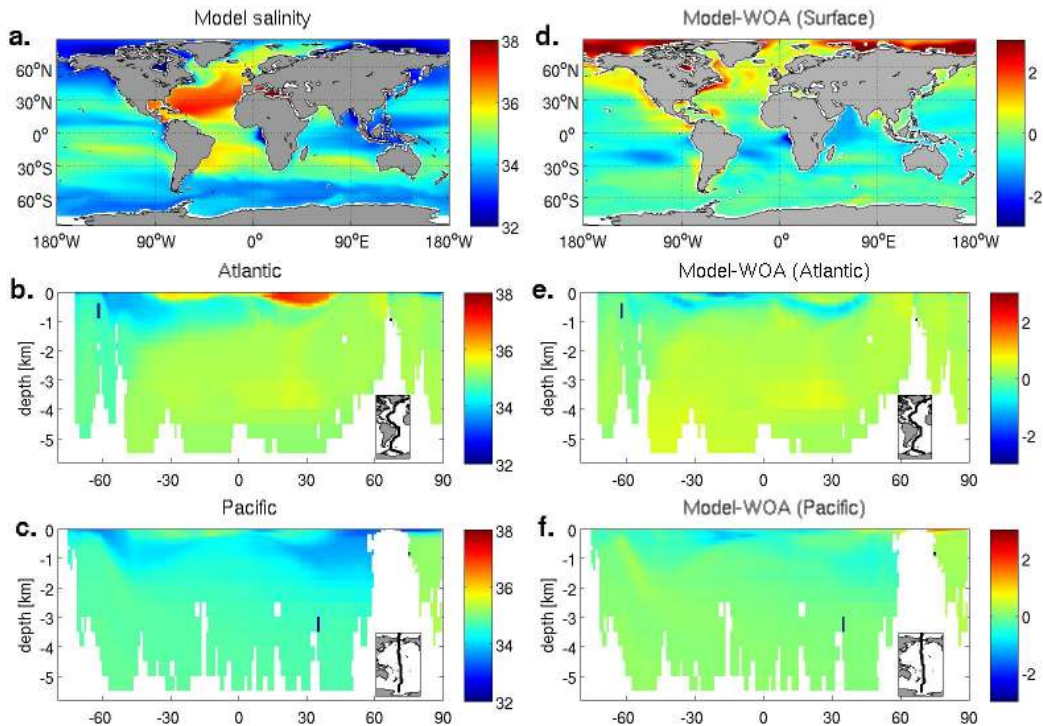
**Fig. 4.** Distribution of ocean salinity from model simulation (left) and difference in salinity between the model and climatological estimates (right) (WOA, Antonov et al., 2010) for the surface (a,d), Atlantic (b,e) and Pacific (c,f) vertical sections. Units are in [psu].

33
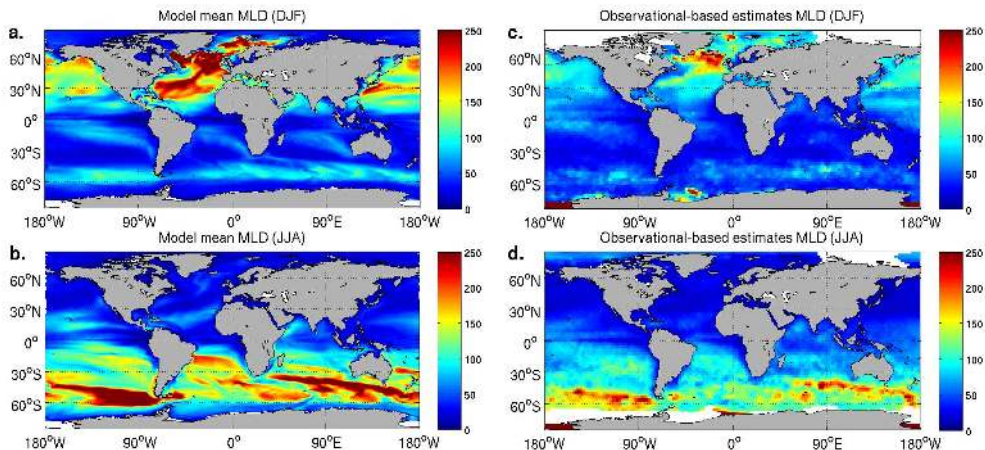
**Fig. 5.** Map of mean mixed layer depth (MLD) from the model (left) and observational-based estimates (right) for boreal winter (December-January-February) and summer (June July August) periods. The model results are computed over the 1991–2000 periods from historical simulation, whereas the observations are adopted from de Boyer Montégut et al. (2004).

34
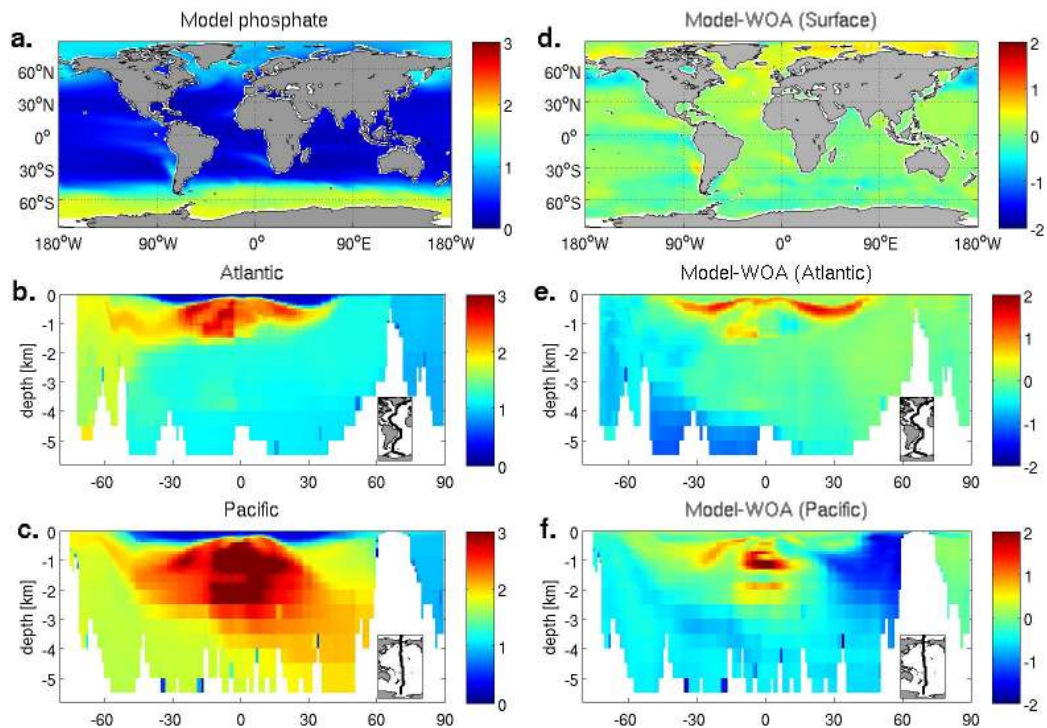
Fig. 6. Distribution of dissolved phosphate concentration from model simulation (left) and difference in phosphate between the model and climatological estimates (right) (WOA, Garcia et al., 2010b) for the surface (a,d), Atlantic (b,e) and Pacific (c,f) vertical sections. Units are in [μmol L^{-1}].
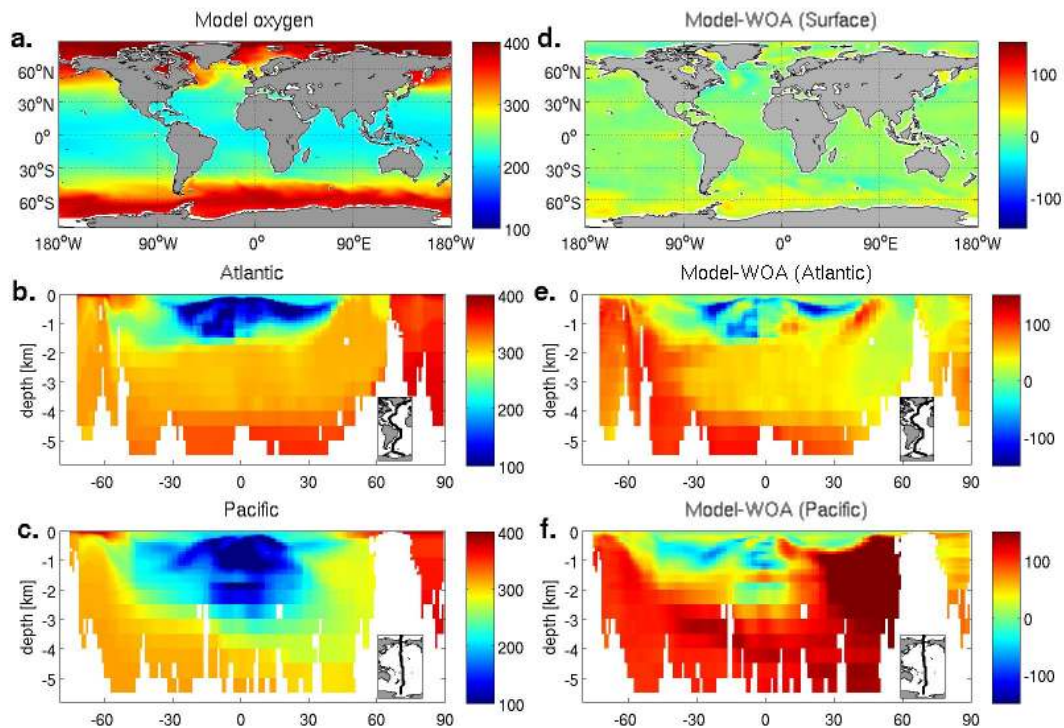
Fig. 7. Distribution of dissolved oxygen concentration from model simulation (left) and difference in oxygen between the model and climatological estimates (right) (WOA, Garcia et al., 2010a) for the surface (a,d), Atlantic (b,e) and Pacific (c,f) vertical sections. Units are in [μmol L^{-1}].
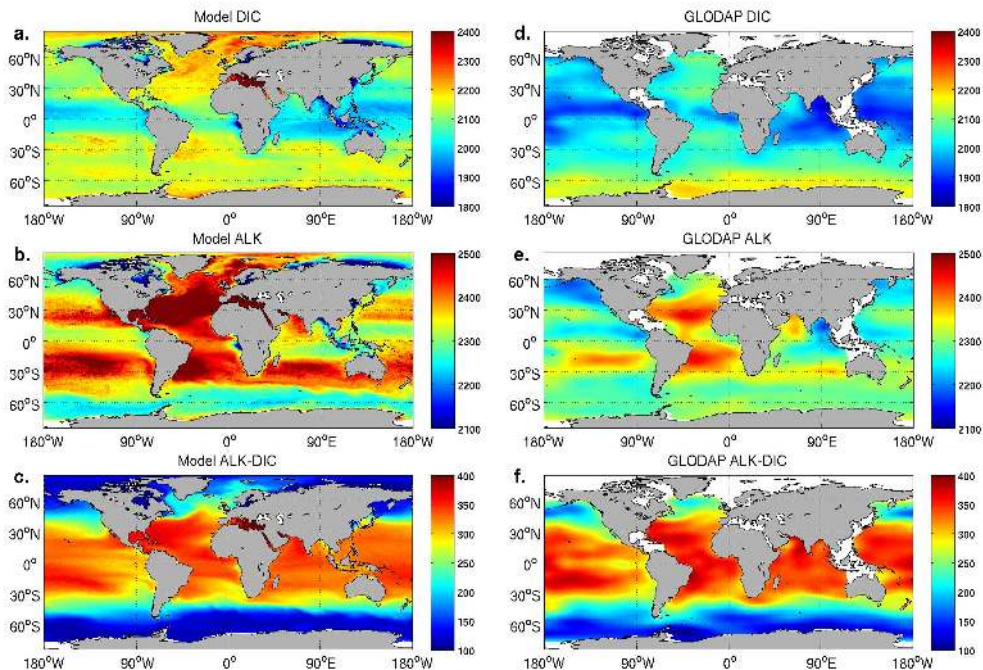
Fig. 8. Model simulated and observed (GLODAP, Key et al., 2004) surface distribution of dissolved inorganic carbon (a,d) and alkalinity (b,e). In addition, we plotted here estimates of carbonate ion concentration taken from subtracted DIC from ALK (c,f). Units are in [μmol kg^{-1}].
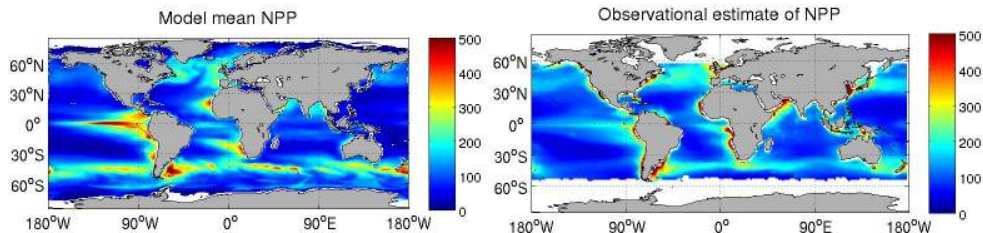
Fig. 9. Model simulated (left) and observed (right) annual mean of surface net primary production. The observation estimate is based on remotely sensed chlorophyll data and the Vertically Generalized Production Model (VGPM) from Behrenfeld and Falkowski (1997). Model value is taken from HIST simulation over 1996–2005 period, whereas the data is from 2003-2007 period. Units are in [g C m^{-2} yr^{-1}].

Table 1. Regional and global annual mean gross primary production (GPP) and terrestrial ecosystem respiration (TER) as simulated by the NorESM and estimated from FLUXNET-MTE data. The FLUXNET-MTE uncertainties were estimated based on global mean uncertainties published by Jung et al. (2011). Units are in [Pg C yr^{-1}]

Regions	NorESM-GPP	FLUXNET-GPP	NorESM-TER	FLUXNET-TER
High latitude north ($>60°$N)	2.6	4.7$\pm$0.8	2.2	3.1$\pm$0.8
Mid-latitude north ($20°$N–$60°$N)	39.8	36.3$\pm$2.7	32.5	29.9$\pm$2.7
Tropics ($20°$N–$20°$S)	75.3	68.0$\pm$1.9	61.9	54.8$\pm$1.9
Mid-latitude south ($20°$S–$60°$S)	12.1	10.3$\pm$0.6	9.9	8.5$\pm$0.6
Global	129.8	119.4$\pm$5.9	106.6	96.4$\pm$6.0
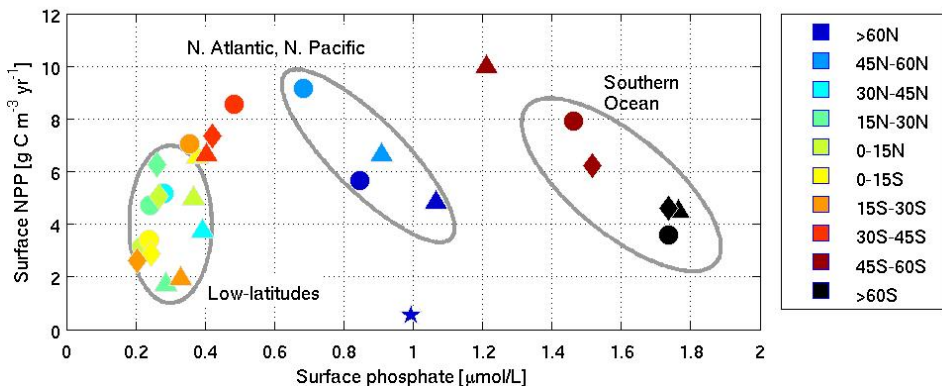
Fig. 10. Latitudinal mean of biological production as a function of mean surface phosphate concentration. The symbols represent different ocean basins: (⋆) Arctic, (◯) Atlantic, (△) Pacific, and (◇) Indian ocean basin.
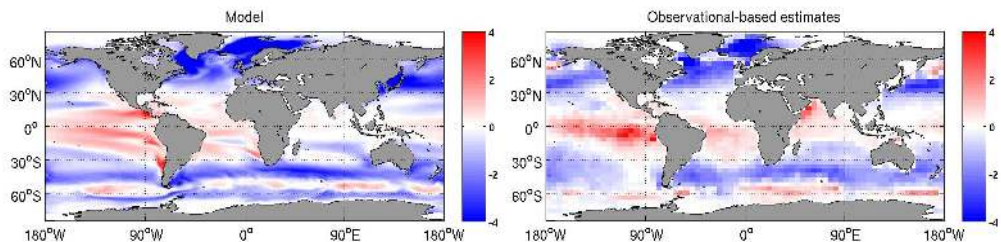

Fig. 11. Map of annual mean sea-to-air CO_2 fluxes for the 1996–2005 period simulated by the model (left) as compared to the observational based estimates (right) of Takahashi et al. (2009). Units are in [mol C m^{-2} yr^{-1}].
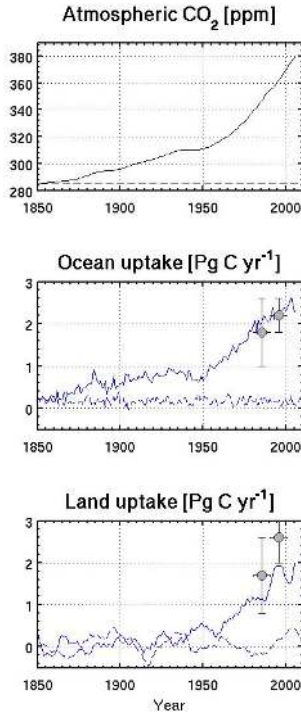
Fig. 12. Time series of atmospheric CO_2 concentration (upper panel), annual oceanic (middle panel), and land (bottom panel) carbon uptake (excluding land use change) simulated over the historical period. Solid lines represent value from HIST, whereas dashed lines represent value from CTRL simulations. Five-years running mean are applied to the land uptake fields. The observation estimates are from Denman et al. (2007).
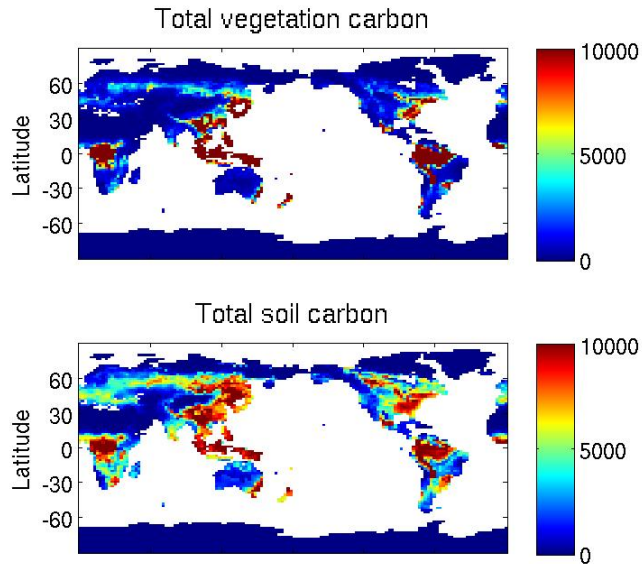
Fig. 13. Maps of mean (top) vegetation and (bottom) soil carbon contents as simulated by the NorESM model. Values are computed over the historical simulation from 1982–2005 period. Units are in [g C m^{-2}].
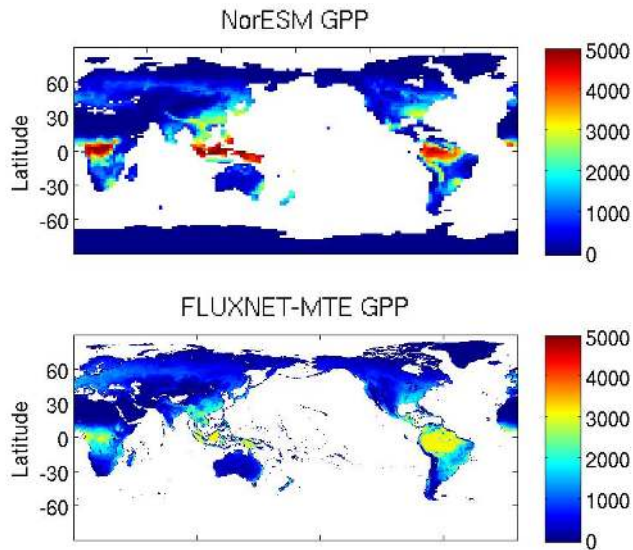
Fig. 14. Maps of mean annual terrestrial gross primary production as simulated by the NorESM model (top) and as estimated from the FLUXNET-MTE observation (bottom). Values are computed from historical 1982–2005 period. Units are in [g C m^{-2} yr^{-1}].
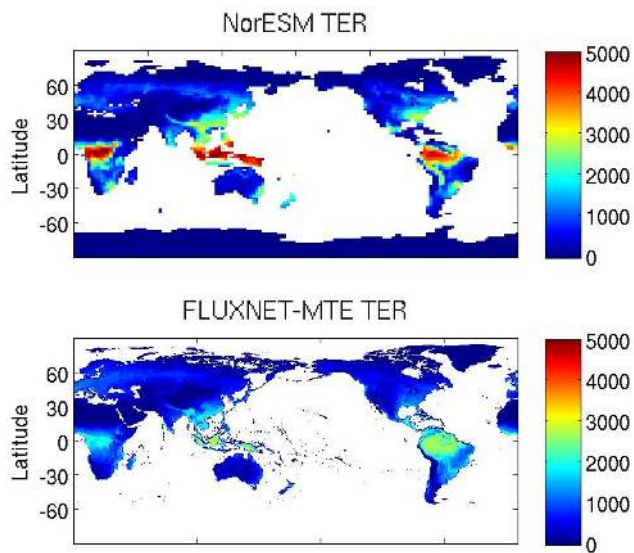
Fig. 15. Same as Fig. 14 for terrestrial ecosystem respiration. Units are in [g C m^{-2} yr^{-1}].
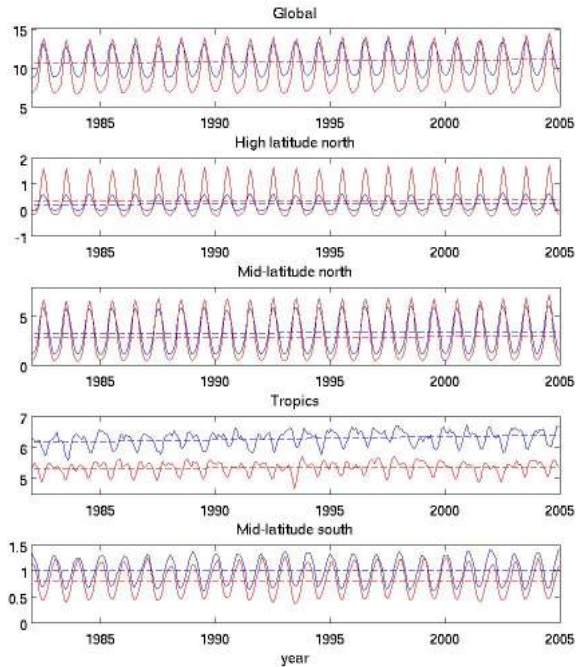
Fig. 16. Time-series of monthly gross primary production (GPP) values simulated by NorESM (blue-lines) as compared to the FLUXNET-MTE estimations (red-lines). Shown are global value, high latitudes (>60°N), mid-latitude north (between 60°N and 20°N), tropics (between 20°N and 20°S), and mid-latitude south (between 20°S and 60°S). The dashed-lines represent the linear trend of the time-series. Units are in [Pg C month^{-1}].